Combined Radiometer–Radar Microphysical Profile Estimations with Emphasis on High-Frequency Brightness Temperature Observations

GAIL M. SKOFRONICK-JACKSON

University of Maryland, Baltimore County, Baltimore, and Goddard Earth Sciences and Technology Center, NASA Goddard Space Flight Center, Greenbelt, Maryland

JAMES R. WANG AND GERALD M. HEYMSFIELD

NASA Goddard Space Flight Center, Greenbelt, Maryland

ROBBIE HOOD

NASA Marshall Space Flight Center, Huntsville, Alabama

WILL MANNING

University of Maryland, Baltimore County, Baltimore, and Goddard Earth Sciences and Technology Center, NASA Goddard Space Flight Center, Greenbelt, Maryland

ROBERT MENEGHINI AND JAMES A. WEINMAN

NASA Goddard Space Flight Center, Greenbelt, Maryland

(Manuscript received 5 February 2002, in final form 25 August 2002)

ABSTRACT

Information about the vertical microphysical cloud structure is useful in many modeling and predictive practices. Radiometers and radars are used to observe hydrometeor properties. This paper describes an iterative retrieval algorithm that combines the use of airborne active and wideband (10–340 GHz) passive observations to estimate the vertical content and particle size distributions of liquid and frozen hydrometeors. Airborne radar and radiometer observations from the third Convection and Moisture Experiment (CAMEX-3) were used in the retrieval algorithm as constraints. Nadir profiles were estimated for 1 min each of flight time (approximately 12.5 km along track) for anvil, convective, and quasi-stratiform clouds associated with Hurricane Bonnie (August 1998). The physically based retrieval algorithm relies on high frequencies ($\geq$150 GHz) to provide details on the frozen hydrometeors. Neglecting the high frequencies yielded acceptable estimates of the liquid profiles, but the ice profiles were poorly retrieved. The wideband observations were found to more than double the estimated frozen hydrometeor content as compared with retrievals using only 90 GHz and below. The convective and quasi-stratiform iterative retrievals quickly reached convergence. The complex structure of the frozen hydrometeors required the most iterations for convergence for the anvil cloud type. Nonunique profiles, within physical and theoretical bounds, were retrieved for thin anvil ice clouds. A qualitative validation using coincident in situ CAMEX-3 observations shows that the retrieved particle size distributions are well corroborated with independent measurements.

1. Introduction

Knowledge of the vertical microphysical cloud structure is important in many aspects of meteorology, such as for determining precipitation rates and latent heating profiles, and for forecasting hurricane intensity (Simpson et al. 1996). In addition, hydrometeor profiles are used to improve global change and cloud-resolving models. Severe storms or intense rain can also affect earth–satellite communication transmissions. For these reasons, accurate estimates of the vertical profile of liquid and frozen hydrometeor particle size distributions are vital to atmospheric research, meteorological, and communications communities. In an effort to estimate precipitation profile information, despite sparsely situated ground-based sensors, airborne- and satellite-based remote sensing instruments have been employed (Kummerow et al. 2000).

The challenge of using airborne or satellite remote

Corresponding author address: Dr. Gail M. Skofronick-Jackson, University of Maryland, Baltimore County, Baltimore, and Goddard Earth Sciences and Technology Center, NASA Goddard Space Flight Center, Code 975, Bldg. 33, Rm. A428, Greenbelt, MD 20771.
E-mail: gailsjackson@ieee.org

sensors is determining the appropriate instruments for the parameter of interest. Infrared instruments provide temperature and relative humidity profiles in cloud-free regions. Lidars can be used to remotely sense cirrus clouds, water clouds, and aerosols (e.g., Wang and Sassen 2002; Savov et al. 2002). However, infrared and lidar instruments cannot be used to reliably obtain detailed precipitating hydrometeor information. A single-channel active microwave radar can only provide one of the two–six key parameters needed to fully characterize the particle size distribution (PSD) at each range gate. A passive multifrequency microwave radiometer allows probing into the different hydrometeor layers of the clouds, and the different channels are sensitive to various hydrometeor types (e.g., liquid vs frozen). The high frequencies ($\geq$89 GHz) of the radiometer are more sensitive to frozen hydrometeors, while the low frequencies are mostly sensitive to liquid hydrometeors. However, radiometers are limited to sensing vertically integrated information about the hydrometeor structure. In addition, the relationships between hydrometeor characteristics and the upwelling brightness temperatures are both nonlinear and nonunique.

By combining active radar and passive radiometers, the opportunities to estimate hydrometeor profiles and cloud characteristics improve (Marzano et al. 1999). In fact, the Tropical Rainfall Measuring Mission (TRMM) (Kummerow et al. 2000) was the first satellite to include both a radar and radiometer designed to measure rainfall. Several radar–radiometer retrieval algorithms have been developed for use with the TRMM satellite (e.g., Olson et al. 1996; Sauvageot 1996; Viltard et al. 2000). Prior to TRMM, most existing remote sensing methodologies for estimating cloud structure independently relied on either radiometer or radar observations (e.g., Meneghini et al. 1997).

Associated with TRMM are calibration/validation field campaigns. One such field campaign was the third Convection and Moisture Experiment (CAMEX-3), which was based in southern Florida during August and September of 1998 (Geerts et al. 2000). The Texas and Florida Underflights (TEFLUN-B) field campaign combined resources with CAMEX-3 with the purpose of underflying the TRMM satellite. Multiple instruments located on the ground, low- and high-altitude aircraft, and satellites were used to observe convective and hurricane systems. Of particular interest for this work are measurements from instruments on the high-altitude Earth Resources-2 (ER-2) aircraft that provided a single active channel at 9.6 GHz and 11 brightness temperature channels ranging from 10.7 to 340 GHz during Hurricane Bonnie on 26 August 1998. The higher-frequency channels are extremely useful for determining and constraining the PSDs of the frozen hydrometeors (Deeter and Evans 2000) and to provide a unique aspect to this work in relation to other combined radar–radiometer retrieval algorithms (e.g., Marzano et al. 1999). Two other CAMEX-3 instruments provide data for retrieval result validation.

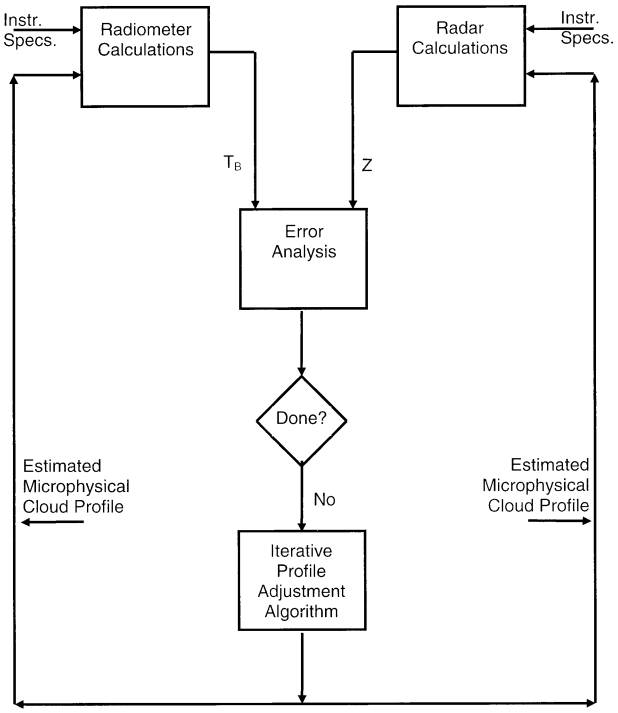

FIG. 1. The retrieval algorithm flowchart.

The purpose of this research is to delineate cloud structures through the retrieval process, not necessarily to propose that all hurricane systems have similar cloud structures. The retrieval algorithm derived herein minimizes the differences between (active and passive) observations and forward calculations based on the iteratively estimated hydrometeor profiles. The observations are used to constrain the solution. In section 2, the retrieval algorithm will be detailed. The application of the algorithm to the CAMEX-3 Hurricane Bonnie data is described in section 3, the corresponding retrieval results and validation in section 4, followed by a summary in section 5.

2. Retrieval algorithm

The retrieval algorithm uses both radar and radiometer observations in the retrieval process. The algorithm emulates the multidimensional downhill simplex method (Nelder and Mead 1965) to minimize the error between observations and calculations based on the iteratively estimated profile. Hydrometeor content and drop size distribution profiles for rain, cloud water, and frozen hydrometeors are adjusted for each iteration. The flowchart of the algorithm is shown in Fig. 1. The flowchart shows that the radar and radiometer calculations are separate, while the error analysis and profile adjustment scheme are combined. Each component in the flowchart is described in detail in this section.

The algorithm is initialized by converting attenuation-corrected (e.g., Hitschfeld and Bordan 1954) nadir-viewed radar reflectivity profiles into estimates of hydrometeor content profiles. The fine (37.5 m) resolution of the radar range gates from 0 to 18 km is averaged to 0.5-km vertical slabs, with 0.1-km resolution between 4.5 and 5.5 km to provide increased resolution near the transition from layers of liquid to frozen droplets. The radar-to-microphysical profile algorithm is initialized using preset temperature, pressure, relative humidity, and cloud water profiles taken from the hydrologically appropriate Goddard Cumulus Ensemble (GCE) (Tao and Simpson 1993) profiles. The hydrometeor content profiles from the radar-to-microphysical profile algorithm are partitioned into liquid and frozen particles with Marshall–Palmer (Marshall and Palmer 1948) and Sekhon–Srivastava (Sekhon and Srivastava 1970) exponential drop size distributions, respectively. While continuity of the precipitation flux across the freezing level is not explicitly enforced, the masses obtained from the radar reflectivities should have smooth transitions from one level to the next. If necessary, hydrometeors in the cloud profile are extended one additional height level above, below, or both above and below the cloud boundaries in order to get nonzero reflectivity (Z) calculations at all nonzero observed Z heights (in this work, Z refers to the reflectivity of the calculations and to the attenuation-corrected Z_m for the observations). The cloud liquid water, rain, and frozen hydrometeor contents and drop size distributions are then adjusted at each iterative stage of the retrieval algorithm.

The retrievals assume a nadir-viewed ocean surface at 300 K. The wind speed is fixed at three different values for the three cloud regions dependent on their distance from the hurricane eye (Anthes 1982). Similar to Marzano et al. (1999), the first 500 m above the ocean surface is not adjusted in the retrieval because of difficulties separating surface radar return from the hydrometeors at those levels.

a. Brightness temperature calculations

An efficient radiative transfer (RT) model is required to transform the microphysical information into upwelling passive microwave brightness temperatures (T_B), which are then compared to observations in the iterative retrieval algorithm. The planar-stratified, scattering-based RT model used herein was originally developed by Gasiewski (1993), and was later modified by Skofronick-Jackson and Gasiewski (1995), to allow for five (or more) hydrometeor types (e.g., suspended cloud water, rain, suspended cloud ice, snow, and graupel). Flexibility exists in that the user can input the cloud profile and select the observation height, viewing angle, frequency (tested from 6 to 425 GHz), and polarization. The RT model requires as input instrument specifications, vertical profiles of temperature, height, relative humidity, and PSD of the hydrometeors in the cloud.

Typically, RT models that handle hydrometeor scattering using a perturbation method (Lenoble 1985), as opposed to the adding–doubling method (van de Hulst 1980), as the model used herein does, require more iterations to reach the final brightness temperature value than the adding–doubling method. An analytical approximation was implemented for this retrieval in order to reduce processing time. The RT perturbation technique sums successive orders of scattering:

$$T_B = \sum_{i=0}^{M} \Delta T_B^{(i)}, \tag{1}$$

where $\Delta T_B^{(0)}$ is the clear air solution and M is preset during the perturbation radiative transfer modeling. The n to M successive orders of scattering can be written in the form of

$$\Delta T_B^{(n)}\left[1 + \frac{\Delta T_B^{(n+1)}}{\Delta T_B^{(n)}} + \frac{\Delta T_B^{(n+2)}}{\Delta T_B^{(n+1)}}\frac{\Delta T_B^{(n+1)}}{\Delta T_B^{(n)}} + \cdots + \frac{\Delta T_B^{(M)}}{\Delta T_B^{(M-1)}}\frac{\cdots}{\cdots}\frac{\Delta T_B^{(n+1)}}{\Delta T_B^{(n)}}\right]. \tag{2}$$

If it can be assumed that $\Delta T_B^{(k+1)}[\Delta T_B^{(k)}]^{-1}$ remains fixed for all $k \geq n$ and $M \to \infty$, then an analytical expression for Eq. (2) is

$$\Delta T_B^{(n)}\frac{1}{1 - W}, \tag{3}$$

where

$$W = \frac{\Delta T_B^{(n+1)}}{\Delta T_B^{(n)}} = \frac{T_B^{(n+1)} - T_B^{(n)}}{T_B^{(n)} - T_B^{(n-1)}}. \tag{4}$$

The $T_B^{(k)}$ are the brightness temperature values at perturbation k. This approximation can cut the number of successive orders of scattering by more than 60%.

It is assumed that a planar-stratified model is acceptable in this work because only high-resolution nadir-viewed observations are used in the retrieval and because the observations have fairly small footprints. Another assumption is that all particles are spherical in shape. While the use of spherical particles is somewhat idealized, this simplification allows the important effects of particle size distribution to be considered separately from that of aspherical particles. Furthermore, since only nadir observations are analyzed in this work, any polarization sensitivity due to aspherical particles is minimized. At high frequencies ($\geq$150 GHz), dielectric mixing theories begin to breakdown because the particle inclusion size becomes electrically large with respect to the wavelength (Sihvola 1989); therefore, frozen hydrometeors are assumed solid ice spheres.

b. Radar reflectivity calculations

The radar reflectivity calculations are based on a model described by Jones et al. (1997). This code is flexible

in that the user can specify the instrument viewing angle and height, radar beamwidth, operating frequency, range gate intervals, etc. The radar model described in Jones et al. (1997) relies on GCE data for input. The standard GCE model runs are performed over a 64 km × 64 km domain with a 1 km × 1 km horizontal resolution and with 19 levels along the vertical. At each of the 64 × 64 × 19 elements, the cloud model provides the water vapor, temperature, and equivalent liquid water contents of rain, graupel, snow, hail, cloud ice, and cloud water at each time step. To compute the drop size distribution of the hydrometeors, an exponential form is assumed with a fixed intercept parameter and mass density. For each particle type, the remaining unknown parameter of the size distribution is calculated from the intercept and the equivalent liquid water contents provided by the GCE model. The radar model uses the extinction and backscattering cross sections of water, snow, and mixed phase hydrometeors obtained from Mie theory, along with the GCE-derived size distributions to compute the effective radar reflectivity at each element of the grid. Last, the backscattered power is computed as a function of range along each radar beam by an integration over the scene weighted with the two-way antenna gain pattern. Effects of surface scattering are taken into account. This radar model has been used to simulate the measurements from the precipitation radar aboard the TRMM satellite and to test various methods of rain-rate retrieval.

For this research, the radar code has been revised to simulate the ER-2 Doppler radar (EDOP) instrument (Heymsfield et al. 1996). The model described in Jones et al. (1997) automatically generates an exponential size distribution and a melting layer; in this work, the retrievals rely solely on the hydrometeor parameterization as iteratively generated by the retrieval. Using the size distributions and the design parameters of the EDOP, the reflectivity is computed at each range gate. By integrating the reflectivity over a simulated radar beam that models the observation radar specifications, the return reflectivity can be calculated and compared to the attenuation-corrected observed data.

c. Error analysis

Once T_B and Z have been computed for the current estimated profile, the error analysis occurs. There are two convergence criteria, one for the T_B and one for the Z:

$$\max[|T_{B\text{obs}}(i) - T_{B\text{calc}}(i)|] < S_{T_B} \quad \text{for all } i \text{ frequencies, and} \tag{5}$$

$$\max[|Z_{\text{obs}}(j) - Z_{\text{calc}}(j)|] < S_Z \quad \text{for all } j \text{ resampled range gates.} \tag{6}$$

The S_{T_B} and S_Z are convergence thresholds and are currently set to 10 K and 2.5 dBZ, respectively. Two convergence criteria are needed so that the brightness temperature and reflectivity errors can be independently analyzed to determine the drop size distribution adjustment needed to reduce any errors. The relatively unknown and highly variable surface conditions (e.g., temperature and sea foam fraction) and frozen hydrometeor states (e.g., sizes, shapes, and densities) necessitate the use of the 10-K brightness temperature threshold. If detailed in situ observations were available, it is expected that the T_B threshold could be reduced or made to be frequency dependent.

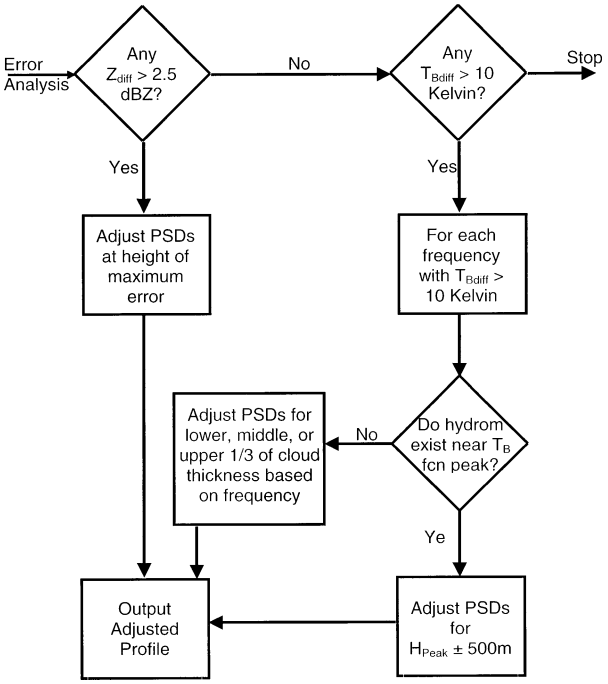

FIG. 2. The size distribution adjustment flowchart.

d. Hydrometeor adjustment algorithm

The hydrometeor adjustment algorithm is outlined in Fig. 2. For each iteration, hydrometeor adjustments are made using the principles of the downhill simplex method (Nelder and Mead 1965). The algorithm first checks to see if the radar convergence criterion is met. If not, the particle size distributions are adjusted at the height h_m of the maximum error in the Z profile. The adjustment factor Y is proportional to the ratio $[Z_{\text{obs}}(h_m)/Z_{\text{calc}}(h_m)]^{\alpha}$, where $\alpha = -0.25$. The Z based adjustments are

$$\Lambda = \Lambda^{\text{old}} Y \quad \text{and} \quad N_0 = N_0^{\text{old}} Y^3 \tag{7}$$

in the exponential PSD equation

$$N(D) = N_0 e^{-\Lambda D} \ (\text{mm}^{-1}\ \text{m}^{-3}), \tag{8}$$

where D and Λ^{-1} are in millimeters and N_0 is in inverse millimeters per meter cubed. This application of Y preserves the T_B values so that they change minimally for Z-based adjustments. If it is assumed that the polydispersive hydrometeors are primarily in the Mie region

with respect to the channel frequencies, then the liquid absorption and the liquid and frozen scattering coefficients are proportional to the content [M (g m^{-3})] divided by the mean diameter $\langle D \rangle$ (Gasiewski 1993). When M is expressed in terms of the size distribution and since $\langle D \rangle = \Lambda^{-1}$, the absorption and scattering coefficients are then proportional to $N_0\Lambda^{-3}$. To maintain these absorption and scattering coefficients, and thus the T_B values, a change of $\Lambda = \Lambda^{\text{old}}Y$ requires the change $N_0 = N_0^{\text{old}}Y^3$. Because it is possible that the particles may be in the Rayleigh region part of the time (and, thus, the above analysis would be invalid), the algorithm requires that the Z errors be corrected before adjusting the profile due to T_B-based errors.

When the convergence criterion for the T_B is not met, a similar adjustment is made to reduce the differences in the observed and calculated T_B values. Frequencies where the temperature difference exceeds 10 K are used to determine where to adjust the hydrometeor profile. Each frequency has a temperature weighting function profile (Gasiewski 1993) that peaks at a height that is dependent on temperature and hydrometeor characteristics. The hydrometeor size distributions are equally adjusted at the heights and $\pm$ one level of where the weighting function peaks for each frequency, with error exceeding 10 K. If the radiometer frequencies are less than 89 GHz, the rain- and cloud-water drop sizes are adjusted; if above 89 GHz, the frozen hydrometeor particle sizes are adjusted. For the 183.3-GHz channels, only the 183.3 $\pm$ 1 GHz channel is used to adjust rain- and cloud-water drop sizes. Errors in the 89, 183.3 $\pm$ 3, and 183.3 $\pm$ 7 GHz channels are usually corrected through PSD adjustments due to errors in other channels.

If the weighting function peak does not fall within the cloud boundaries, the particle size adjustments cannot be performed at the weighting function peak. Thus, the adjustments are made to the lower, middle, and upper third of the cloud volume based on the frequency and the channel's relative sensitivity to the hydrometeor types and their typical locations within a cloud. For 37 and 150 GHz, particle sizes within the lower third of the cloud liquid and frozen hydrometeor layers (respectively) are adjusted. For 183.3 $\pm$ 1 and 220 GHz, the particle sizes within the middle third of the cloud liquid and frozen hydrometeors (respectively) are adjusted. Last, for 340 GHz, the particle sizes in the upper third of the frozen hydrometeor layers in the cloud are adjusted.

The adjustment parameters are a function of the ratio $[T_{B\text{obs}}(k)/T_{B\text{calc}}(k)]^{-\beta}$ denoted by X, where k is the index of the frequency at which an error occurs and β is dependent on the hydrometeor and height level to be adjusted. For this work, β is 3/7, 2.5/7, 2/7, and 0.5/7 for $\leq$ 183.3 $\pm$ 1, 150, 220, and 340 GHz, respectively. The sensitivity to ice increases for the higher frequencies and, thus, the β factor must prescribe smaller changes for these higher frequencies. While the β are fixed over the three storm types retrieved herein, it is possible that the β may change under other storm system conditions. The T_B-based adjustments are

$$\Lambda = \Lambda^{\text{old}}X \quad \text{and} \quad N_0 = N_0^{\text{old}}X^7 \tag{9}$$

in the exponential PSD Eq. (8). This application of X preserves the Z values because Z is proportional to $N_0\Lambda^{-7}$ [recall that $Z \propto \int D^6N(D)\,dD$].

The adjustments to the size distributions of a specific height level and hydrometeor type are only changed once per iteration. This eliminates the scenario where one adjustment for a frequency or range gate would cancel out the adjustment for a different frequency. Also the adjustments do not preserve the content of the hydrometeors because the M is proportional to D^4N_0. While we have been able to meet our convergence criteria for anvil, convective, and stratiform cloud cases, it is likely that further improvements to the adjustment algorithm will allow us to tighten the convergence criteria thresholds.

3. Application to CAMEX-3 data

Observations from CAMEX-3/TEFLUN-B (Geerts et al. 2000) are used in the retrieval algorithm. While CAMEX-3 had broad-based instrumentation on multiple platforms, including aircraft, ground, ship, and satellite, this work focuses on the data from four instruments on the ER-2 aircraft and one instrument on the DC-8 aircraft. On board the ER-2, flying at an altitude of 20 km, the instruments of interest for this work are the Millimeter-wave Imaging Radiometer (MIR) [Racette et al. (1996)], the Advanced Microwave Precipitation Radiometer (AMPR) [Spencer et al. (1994)], the EDOP [Heymsfield et al. (1996)], and the National Polar-Orbiting Operational Environmental Satellite System (NPOESS) Aircraft Sounder Testbed—Microwave (NAST-M) [Blackwell et al. (2001)]. These ER-2 instruments measure atmospheric hydrometeors in the microwave region of the electromagnetic spectrum. The MIR observes at 89; 150; 183.3 $\pm$ 1, $\pm$3, $\pm$7; 220; and 340 GHz, while the AMPR observes at 10.7, 19.35, 37, and 85.5 GHz. The EDOP is an active radar sampling at 9.6 GHz with a range gate interval of 37 m. The NAST-M, used only for validation purposes, is a passive microwave spectrometer with 17 channels near the oxygen absorption lines at 50–57 GHz and 118.75 GHz. The NAST-M channels are independent of any channels used in the retrieval. On the DC-8 aircraft, flying at 12-km altitude, there is the Particle Measuring Systems, Inc., (PMS) 2D-C cloud probe as part of the Cloud and Aerosol Particle Characterization (CAPAC) suite of instruments. The PMS 2D-C probe provides in situ observations of particle size distributions used to check the retrieved size distributions. The 2D-C probe measured PSDs from about 30 μm to above 1 mm in 30-μm increments (McFarquhar and Heymsfield 1997).

For this work, only the nadir or near-nadir signatures are used. The datasets from the MIR, AMPR, and EDOP

have been analyzed and collocated. In an effort to match each radiometer channel and the corresponding EDOP radar samples to similar volumes of the storm, all data values were simulated to match the lowest-resolution channel of all the instruments. The largest footprint of 2.8 km occurs for the AMPR 10- and 19-GHz channels at nadir when the ER-2 is flying at a 20-km altitude. Because there is not an AMPR pixel directly at nadir, for the 10- and 19-GHz channels, the two pixels adjacent to nadir were averaged in an effort to simulate a nadir value. In order to transform the MIR, EDOP, and the higher-frequency AMPR data to the lowest resolution, a two-dimensional Gaussian-weighted mean for each set of data values is calculated where the weights are 1.0 at the center and 0.5 at 1.4 km away from the center. Additionally, because the EDOP radar does not sample off nadir, it probably misses some of the volume sample that the radiometers observe. The EDOP has a 3° beamwidth, so it is observing about 0.6 km off nadir in both directions at the surface instead of the 1.4-km off-nadir view of the AMPR 10- and 19-GHz channels.

While checking the quality of the match between the instruments, an offset between the AMPR 85-GHz channel and the MIR-89 GHz channel was observed. Even though the quantitative values of the brightness temperatures of these two channels are not expected to match exactly, it is reasonable to assume that the time series of the brightness temperature trend for the two channels should be similar. It was determined that the value of the offset in time was dependent upon ER-2 altitude and airspeed; therefore, a pointing angle difference was hypothesized as the cause of the error. This pointing angle difference was consistently determined to be 3.3° when using three separate sets of field campaign data for MIR and AMPR from the 1998 CAMEX-3 and 1999 TRMM Large-scale Biosphere–Atmosphere Experiment in Amazonia (LBA) time period. The cause of this error is likely related to slight differences in the orientation of instruments within the ER-2 aircraft. The correlation of the time series of the EDOP and AMPR data was determined to be acceptable, so no correction was applied to these data; MIR data were corrected using the pointing angle difference along with the ER-2 altitude and airspeed values.

Figure 3 shows the collocated observed data for Hurricane Bonnie on 26 August 1998, including EDOP data (upper panel), MIR brightness temperatures (middle panel), and AMPR brightness temperatures (lower panel). For this image, the ER-2 is flying west to east at approximately 32.8°N latitude. The left-hand side of the image corresponds to the outer edge of Hurricane Bonnie, and the plane is flying toward the eye. The hurricane eye is about 4.5 flight minutes (~55 km) beyond the right-hand side of the image. There are at least three distinct cloud types in Fig. 3: an anvil cloud region on the left of the image (from 1404:00 to about 1407:30 UTC) with a high altitude EDOP reflectivity profile and low brightness temperature values for the MIR frequencies (indicating cooling from ice scattering). There is a weak outer eyewall-embedded convective core from about 1411:00 to about 1413:30 UTC and a quasi-stratiform cloud region from about 1415:20 to about 1417:00 UTC. The quasi-stratiform, convective, and anvil regions are about 75, 115, and 215 km away from Hurricane Bonnie's eye, respectively. These distances away from the eye correspond to surface wind speeds of approximately 35, 30, and 15 m s^{-1} for the quasi-stratiform, convective, and anvil regions, respectively (Anthes 1982).

The retrieval algorithm focuses on small regions within these three storm types. The selected times span from 1405:04–1406:05, 1412:07–1413:41, and 1415:40–1416:38 UTC for the anvil, convective, and quasi-stratiform regions, respectively (see Figs. 4a,b). The path integrated attenuation for these three regions is small (less than 2–3 dB), except around 1413:00 UTC where it is about 8 dB. Nevertheless, the attenuation in the EDOP reflectivity shown in Fig. 4a has been corrected using the Hitschfeld and Bordan (1954) technique. The temporal sampling of the collocated dataset is about 3 s and has a footprint size of 2.8 km at the ER-2 altitude of 20 km. However, because the observations are oversampled, the retrieved profile footprints are between 12.5- and 18.7-km along track of the flight line, for a total of ~44 km analyzed cross track. An analysis of the complete dataset as shown in Fig. 3 is computationally prohibitive at this time and would require additional adjustments to the size distribution adjustment algorithm for the transitioning cloud-type regions. These selected times, although a minimal dataset, will provide a measure of how effective the retrieval is in three different cloud types.

4. Retrieval results

The iterative retrieval algorithm was used to estimate the vertical hydrometeor profiles of the three storm types found within Hurricane Bonnie's outer rainbands. The retrieval performed well, producing extremely good matches between the observed and calculated Z (see Figs. 4a,b). The brightness temperature matches were less than the maximum threshold of 10 K for all of the cases (see Fig. 5). The average number of iterations required for estimating one profile was 36, with the anvil retrievals requiring more iterations than the average number to converge and the quasi-stratiform case requiring fewer than the average number of iterations to converge. In general, it was easiest to reach convergence for the radar reflectivity–stopping criterion and more difficult to reach convergence for the high frequencies of the radiometer. This is reasonable because the initial estimated profiles were obtained by transforming the EDOP reflectivities to hydrometeor content profiles. Additionally, the high-frequency radiometer channels are quite sensitive to the frozen hydrometeor size distributions, which are not well known and, therefore, make

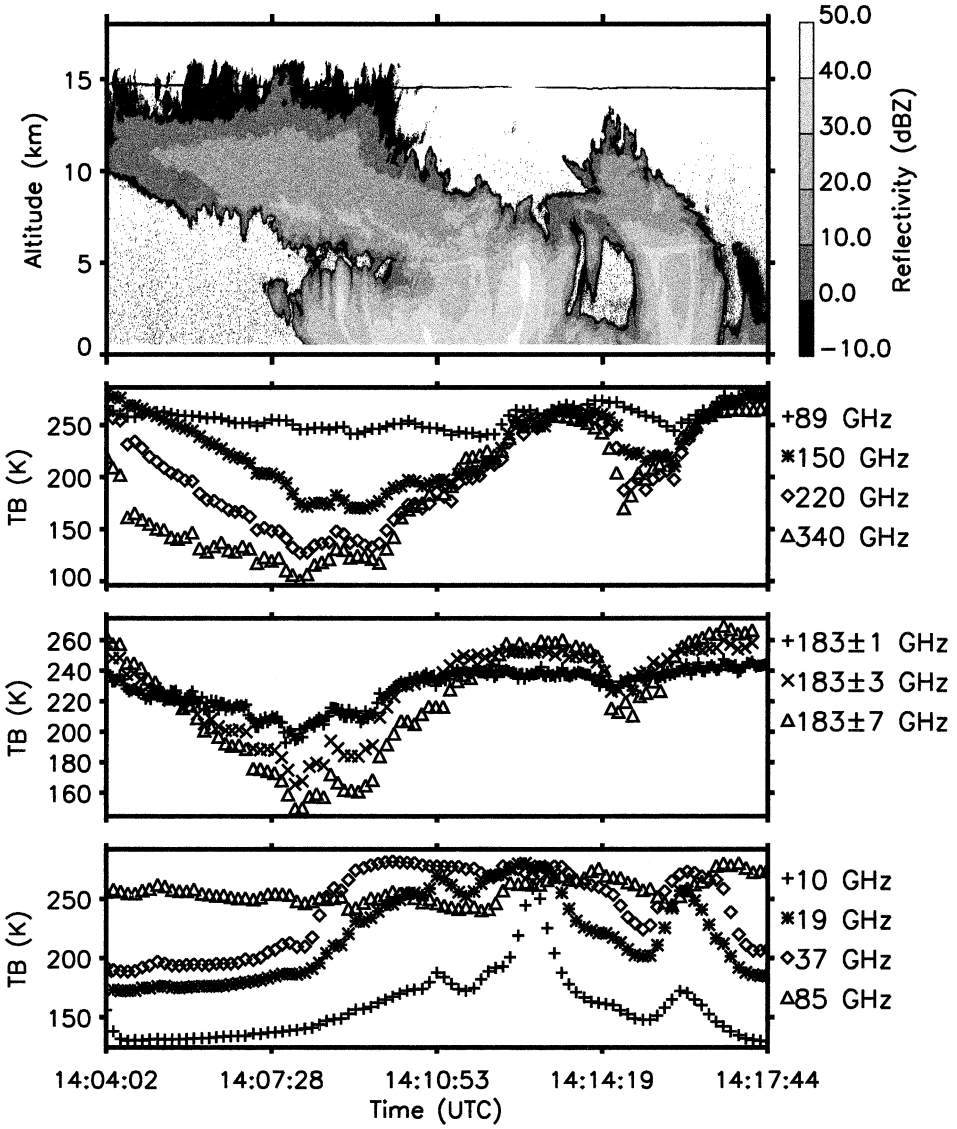

FIG. 3. The (top) EDOP radar reflectivity, (center two) MIR brightness temperatures, and (bottom) AMPR brightness temperatures.

it difficult to ascertain the proper sizes to obtain a good match between the high-frequency observations and calculations. Finally, it must be stated that some of the retrieved profiles are not unique solutions for the observed data. In particular, the anvil cases had two or more slightly different PSD profiles that still met the convergence criteria (see Fig. 6a). It is assumed that if the convergence criteria were even more restrictive, the differences in the retrieved profiles would decrease. Even though the retrievals may not be unique, they still provide good approximations to the actual cloud structure and hydrometeor size distributions.

a. Anvil results

For the anvil case (1405:04–1406:05 UTC), output from the estimated profiles are shown in Figs. 4c–f (left-hand side of each image). Figures 4c and 4e show the liquid and frozen hydrometeor contents, and Figs. 4d and 4f show the liquid and frozen (melted) hydrometeor median diameter [$D_0 = 3.67\Lambda^{-1}$ from Eq. (8)]. The algorithm also produces the number density [N_0 from Eq. (8)] but this value is not plotted because it can be extracted using the content M and Eq. (8) in

$$M = \int_0^\infty N(D)\frac{\pi D^3}{6}\rho \, dD, \tag{10}$$

where $\rho = 1.0$ g cm^{-3} for rain and 0.917 g cm^{-3} for the frozen hydrometeors.

In Fig. 4e, notice that the frozen hydrometeor content variability is large across the whole anvil region. The variability can be attributed to the difficulties in reaching convergence for the anvil region profiles. In the anvil

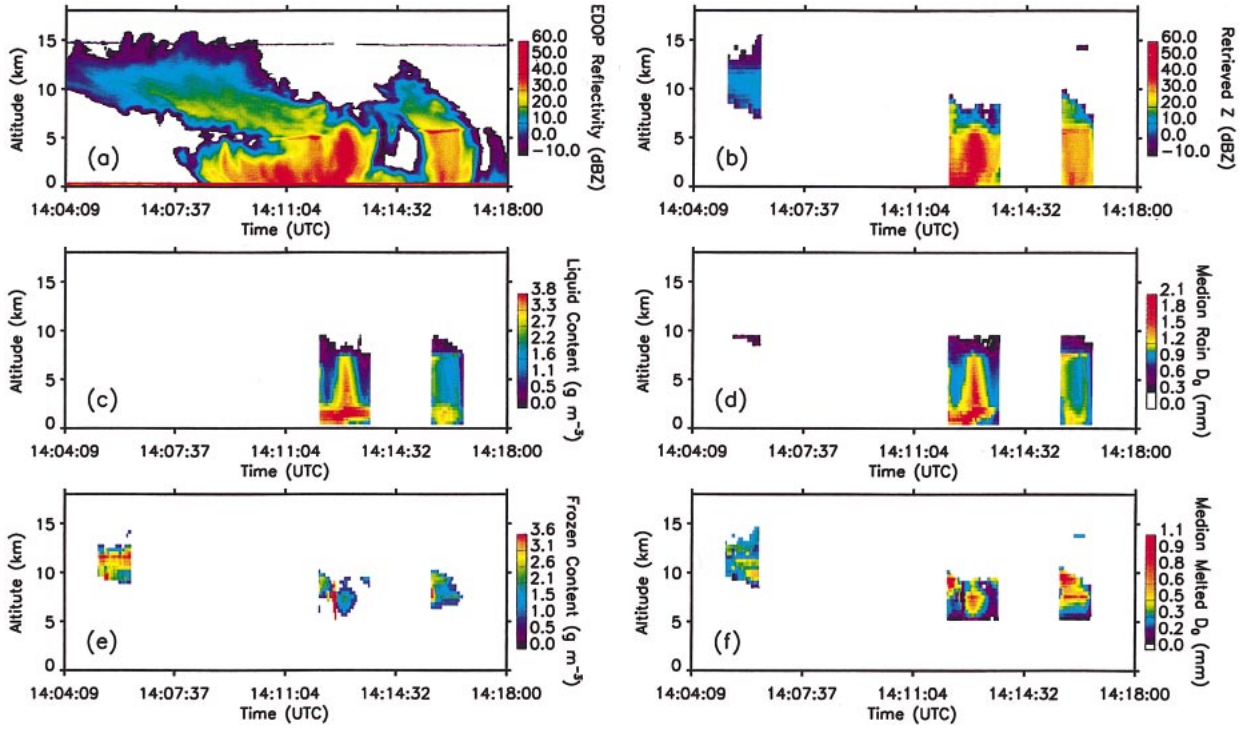

FIG. 4. The (a) EDOP radar reflectivity, (b) calculated reflectivity for the retrieved profile, (c) retrieved liquid water content, (d) retrieved rain median diameter, (e) retrieved frozen content, and (f) retrieved frozen hydrometeor median melted diameter.

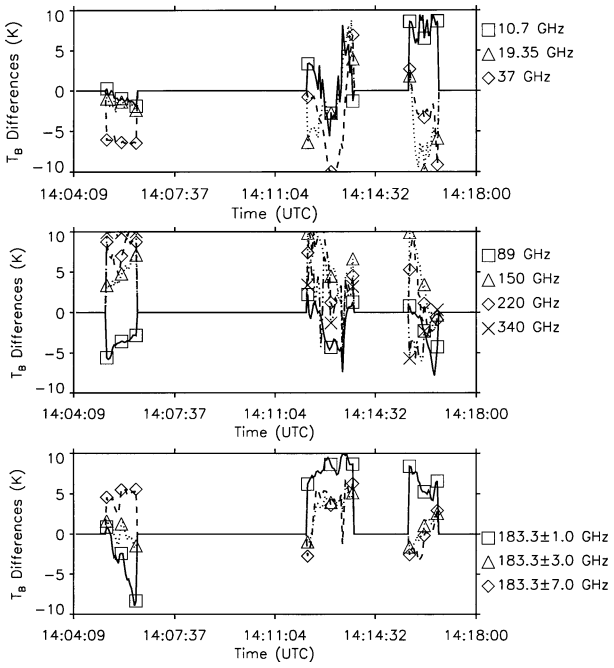

FIG. 5. The calculated minus observed brightness temperatures differences for (top) low frequencies, (middle) high frequencies, and (bottom) 183.3-GHz channels.

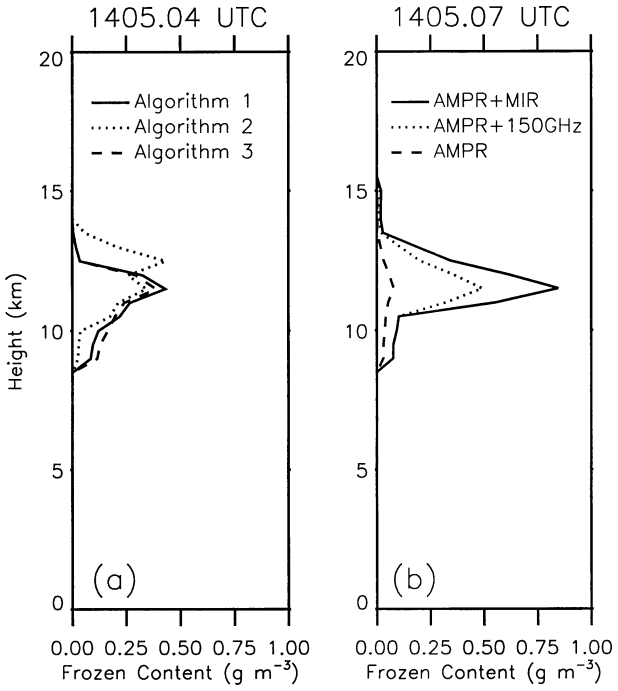

FIG. 6. Single profile retrieval results for (a) different hydrometeor adjustment retrieval algorithms and (b) EDOP data plus a reduced microwave channel set.

region, the median diameter of the liquid and frozen (melted diameter) particles does not exceed 0.16 and 0.56 mm, respectively. The average (over all heights and UTC in the anvil cloud) melted median diameter is 0.077 mm. The radar and radiometer calculations extend the exponential drop size distribution to approximately 3 times these median diameters.

Figure 5 shows the differences in calculated and observed T_B. As can be seen from Fig. 5 (left-hand side), the differences for the 340-GHz brightness temperatures bound the convergence criterion space. The average number of iterations required for estimating an anvil profile is 78. The required number of iterations is higher than the other cases because of the difficulty in determining appropriate characteristics for the frozen hydrometeors. In addition, the assumption of solid ice spheres here, rather than specific crystalline shapes or fluffy snow, may increase convergence time. It is expected that once in situ observations can be used to characterize the frozen hydrometeor state, more profiles can be found that will produce T_B and Z that fall within the convergence criteria.

In the anvil region, there is a negative bias where the calculations of T_B are too cool for the low frequencies and have a positive bias for the highest frequencies. It is possible that the contents of the monodisperse cloud water and cloud ice initialized by the GCE model are not properly estimated. (Note that cloud water content, but not cloud ice content, is adjusted in the retrieval.) Early tests using cloud water and cloud ice from other cloud models do not improve the retrieval results significantly. Modifying the retrieval algorithm to adjust the cloud water and cloud ice presents several difficulties: 1) the radar data is not sensitive to cloud water and cloud ice, 2) the cloud water and cloud ice may extend beyond the boundaries of the radar returns strongly enough to indicate the presence of clouds, and 3) should cloud water and cloud ice be modeled monodispersedly or polydispersedly. Furthermore, the low frequencies are particularly sensitive to the surface conditions and low-altitude hydrometeors. This issue with underestimated low frequencies is further compounded because the retrieval algorithm does not adjust the hydrometeors in the region between the earth's surface and 500 m up because it is difficult to separate surface radar return from hydrometeors at those levels.

Figure 6a shows that the anvil profile retrievals may not be unique. This is not surprising because the relationships between the profiles and the T_B and Z are nonlinear and underconstrained. Furthermore, the complexity of determining a unique profile is increased because in this work there are over 400 profile and surface variables that contribute to the computed T_B and Z values. Nevertheless, Fig. 6a shows the retrieved profile for 1405:04 UTC for three different size distribution adjustment algorithms (modifications to Fig. 2). Algorithm 1 is used for the results reported in this paper. All three algorithms met the convergence criteria and are within the intrinsic microphysical (McFarquhar and Heymsfield 1997) and theoretical (Skofronick-Jackson et al. 2002) variability of frozen hydrometeors; however, algorithm 2 tended to put more ice at upper altitudes and less at lower altitudes. Although the anvil profiles are different, the columnar ice masses among the three algorithms are within 0.1 kg m^{-2} of each other. We expect the integrated mass contents to be relatively consistent among the nonunique retrievals for each estimated profile. Although it is not shown in the figures, it must be stressed that the retrieved profiles for the three algorithms are much more similar for thicker anvil, convective, and stratiform clouds. The nonunique retrieved profiles for thin anvil ice are not surprising because 1) the EDOP radar is relatively insensitive to these ice sizes and 2) the relationships between frozen hydrometeors and high-frequency T_B are not fully understood.

For anvil clouds the necessity of using the high-frequency channels to determine frozen hydrometeor characteristics is shown in Fig. 6b. This figure shows what happens when the retrieval algorithm does not utilize (i.e., correct for errors in) the high-frequency channels. For the single profile at 1405:07 UTC, the solid line in Fig. 6b shows the results using all available data. For this figure, the solid line is considered the truth. The dotted line shows the retrievals using only EDOP and frequencies less than and equal to 150 GHz. The dashed line shows the results when using only EDOP and frequencies less than or equal to 89 GHz. For the low-frequency case (dashed line), the calculated T_B for the 340-GHz channels are 60–70 K warmer than the observations. Clearly, much information about frozen hydrometeor content cannot be derived when only the low-frequency channels are used.

b. Convective results

The convective profiles (1412:07–1413:41 UTC), on average, required fewer iterations (25). This is due to the underlying rain profile stabilizing the low-frequency radiometer data and reducing the impact of the ocean surface conditions. Figures 4 and 5 (center region) show the retrieved content, median diameter, and T_B differences. Figure 4 indicates liquid and frozen contents similar to what would be expected for the EDOP profile (Fig. 4a). The maximum median drop diameter for rain (over all nonzero retrieved rain pixels) is 0.58 mm; for the frozen hydrometeors the maximum melted median drop diameter is 1.1 mm. It is encouraging that the frozen hydrometeors (Figs. 4e,f, center convective region) follow the pattern seen in the reflectivity observations.

The T_B differences in Fig. 5 show much variability. However, the high-frequency calculations (from retrieved profiles) tend to be warmer than the observations. Again, this may imply that the cloud ice is not adequately modeled. The low-frequency T_B difference

variability indicates surface and near-surface variability that is not easily retrieved.

c. Quasi-stratiform results

The quasi-stratiform retrievals met the convergence criteria in just nine iterations (on average). There are two reasons for the quick convergence: 1) a uniform cloud structure and 2) the initialization procedure did a good job estimating liquid and the few frozen hydrometeor levels of this storm, indicating that the Marshall and Palmer (1948) PSD is reasonably appropriate for this quasi-stratiform cloud. Once again, content and median diameter profiles are shown in Fig. 4 (right-hand side) and T_B differences are shown in Fig. 5. The maximum median diameter is 0.39 and 1.03 mm for liquid and frozen hydrometeors (melted), respectively. These retrieved profiles are likely nonunique because when the frozen particles are modified to be more realistic (e.g., including a melting layer), other acceptable profiles will emerge.

The frozen hydrometeor content of the quasi-stratiform region shown in Fig. 4 follows the EDOP reflectivity profile (e.g., more ice on the left-hand side of the quasi-stratiform region and a peak diameter band at the melting layer height). Note that the brightband height increases toward the right as we move toward the hurricane eye. This is typical because the temperatures are warmer in the eye. The T_B differences are revealing: there is a trend of improved comparisons between high-frequency observed and calculated T_B values near the center of the quasi-stratiform time segment (1415:40–1416:38 UTC). At the fringes of the time segment there is a steep decrease of rain and/or frozen hydrometeors, as shown in the EDOP image. Within these highly variable regions it is more difficult to match the observed and calculated T_B.

d. Validation of retrieval results

Because the true microphysical profile cannot be measured at the spatial and temporal scales appropriate for the nadir-viewed ER-2 aircraft brightness temperature observations, qualitative verification of the retrieved profiles will have to suffice. Two different sources of CAMEX-3 coincident information are used to check the results: 1) the passive brightness temperature oxygen band channels on the NAST-M (Blackwell et al. 2001) and 2) the in situ observations at ~12 km from the DC-8 aircraft CAPAC 2D-C probe.

First, the 50.3 ± 0.09- and 118.75 ± 3.5-GHz NAST-M channels were compared to calculations at those same frequencies using the retrieved profiles. These two channels represent the NAST-M channels farthest away from the oxygen line centers and, thus, more sensitive to the hydrometeors in addition to the oxygen. The NAST-M instrument is on board the ER-2 sampling the same (nadir-viewed) scene as the EDOP, MIR, and AMPR.

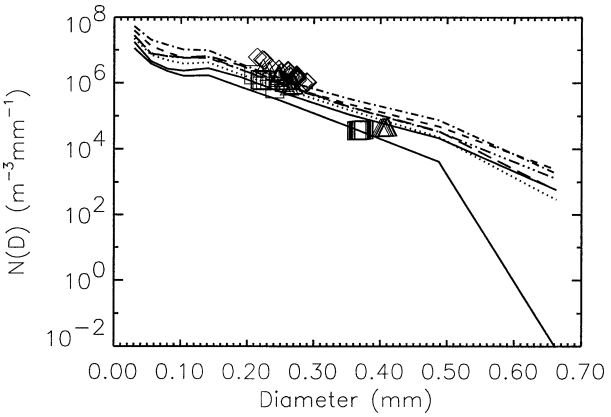

FIG. 7. CAPAC PMS 2D-C in situ observations from the DC-8 flying at 12-km altitude for 1400–1406 UTC (lines), and retrieved anvil $N(D)$ for $D = D_0$ at 11.5 (diamonds), 12.0 (triangles), and 12.5 km (squares).

Because the NAST-M channels were not resampled to the grid of the combined EDOP–MIR–AMPR observations, there were fewer overlapping samples. Each of the calculated T_B values using the retrieved profile for these overlapping UTC was less than 10 K different from the NAST-M values. This means that the retrieved profiles are consistent (in terms of the convergence criteria) with T_B values of the outermost wings of these oxygen bands.

The second validating dataset is from the CAPAC suite of in situ microphysical measurement instruments observing from the DC-8 aircraft during CAMEX-3; the PMS 2D-C probe was the primary instrument of interest here. The DC-8 flies at a height of about 12 km (8 km below the ER-2), and for this UTC segment was well correlated with the ER-2 flight path. Because 12 km is above the cloud tops of the convective and stratiform regions retrieved herein, the 2D-C microphysics data can only be used to validate anvil ice characteristics. The 2D-C probe images particles within its field of view, which are then processed to produce the number of particles in specified bin sizes within a centimeter-cubed volume of air. While it might be interesting to validate hydrometeor mass content, to do so would require introducing additional assumptions about the particle density as a function of size. Thus, only particle size distributions are validated. To compare these measurements with the retrieved exponential PSDs, the number of particles in the centimeter-cubed volume were divided by the interval size of the diameter bin sizes. This provides a number considered equivalent to $N(D)$ for each of the diameter bin sizes. The retrieved N_0 were then multiplied by e^{-1} to provide a value of $N(D)$ at $D = D_0$ in Eq. (8). To reduce the sampling volume of the remote sensors, only the retrieved PSDs at 11.5, 12.0, and 12.5 km were used in the validation comparison. Figure 7 shows the comparison of PMS 2D-C data for 1400–1406 UTC (the DC-8 was underflying the ER-2 for these

UTC) to the retrieved anvil ice at 11.5–12.5 km. This figure shows that the retrieved values (symbols for each height) are very similar to the PMS 2D-C data (lines for each UTC). This qualitative validation indicates that the anvil ice retrievals are close to the in situ observations.

5. Summary

This paper has provided retrieval estimates of precipitation profiles and frozen hydrometeor profiles when using wideband radiometer observations plus radar observations. Profiles of hydrometeor characteristics were estimated using an iterative retrieval algorithm. The algorithm minimized the differences between forward calculations and observed radar and radiometer observations from the ER-2 aircraft obtained during CAMEX-3. The advantages of this retrieval algorithm are 1) the use of high-frequency channels to provide details of the frozen hydrometeors, and 2) combining radar and radiometer observations.

Contents and particle size distributions for spherical rain, cloud water, and frozen hydrometeors were estimated for profiles extending to 18 km with vertical spacing of 0.5 km. The retrieval was performed on anvil, convective, and quasi-stratiform cloud types. Surface winds speeds were varied for the three regions depending on their distance from Hurricane Bonnie's eye. The anvil cloud type required the most iterations in order to resolve the unknowns related to the characteristics of the frozen hydrometeors. The quasi-stratiform region met the convergence criterion the quickest because the initialization procedure used drop sizes more applicable to stratiform cloud types.

The retrieval results were qualitatively compared using observations from the NAST-M on the ER-2 and the CAPAC 2D-C probe on the DC-8 aircraft. The brightness temperatures of the outermost wings of the 50–60- and 118-GHz oxygen bands, as measured by the NAST-M, were within the convergence criteria (less than 10 K from the calculated brightness temperature values). Likewise, observations from the PMS 2D-C probe on the DC-8 aircraft flying at 12 km above the earth's surface were used to validate the particle size distributions of the anvil region retrievals. The retrieved anvil particle sizes and number densities matched the measured 2DC probe microphysics well. Unfortunately, the DC-8 was above the cloud tops for the convective and quasi-stratiform regions and no validation using the PMS 2D-C data could be performed for them.

The retrieved profiles contain considerable information about the cloud structure and hydrometeor size distribution profiles. More importantly, this work shows that high-frequency microwave channels ($\geq$150 GHz) provide information needed in order to define the frozen hydrometeor characteristics found at the upper-altitude levels of a cloud. Even though the retrieved anvil profiles may not have unique frozen hydrometeor characteristics, the range of solutions is relatively insignificant with respect to estimates of precipitation rate, hurricane intensity, and latent heating profiles. With additional analysis this research can be used to improve cloud-resolving and global change models. Furthermore, this work shows that high-frequency microwave channels ($\geq$150 GHz) provide information needed in order to define the frozen hydrometeor characteristics found at the upper-altitude levels of a cloud.

Acknowledgments. This work has been supported by Ramesh Kakar through the NASA Tropical Rainfall Measuring Mission (NAG5-7777, NAG5-10347). The authors thank Phil Rosenkranz for the NAST-M data. We thank Rudolf Pueschel, Anthony Strawa, and Robert Black for the CAPAC PMS 2DC probe data, which was obtained online at http://ghrc.nsstc.nasa.gov/camex3/qlook.html. We also thank the Global Hydrology Resource Center and NASA Earth Sciences Enterprise/Atmospheric Dynamics Program for all of the CAMEX-3 data. Lin Tian was invaluable in analyzing the effects of attenuation in the EDOP reflectivities. We also thank the reviewers for their comments that improved this paper.

REFERENCES

Anthes, R. A., 1982: *Tropical Cyclones—Their Evolution, Structure, and Effects. Meteor. Monogr.,* No. 41, Amer. Meteor. Soc., 208 pp.

Blackwell, W. J., J. W. Barrett, F. W. Chen, R. V. Leslie, P. W. Rosenkranz, M. J. Schwartz, and D. H. Staelin, 2001: NPOESS aircraft sounder testbed-microwave (NAST-M): Instrument description and initial flight results. *IEEE Trans. Geosci. Remote Sens.,* **39,** 2444–2453.

Deeter, M. N., and K. F. Evans, 2000: A novel ice-cloud retrieval algorithm based on the Millimeter-Wave Imaging Radiometer (MIR) 150- and 220-GHz channels. *J. Appl. Meteor.,* **39,** 623–633.

Gasiewski, A. J., 1993: Microwave radiative transfer in hydrometeors. *Atmospheric Remote Sensing by Microwave Radiometry,* M. A. Janssen, Ed., John Wiley and Sons, 91–144.

Geerts, B., G. M. Heymsfield, L. Tian, J. B. Halverson, A. Guillory, and M. I. Mejia, 2000: Hurricane Georges's landfall in the Dominican Republic: Detailed airborne Doppler radar imagery. *Bull. Amer. Meteor. Soc.,* **81,** 999–1018.

Heymsfield, G. M., I. J. Caylor, J. M. Shepherd, W. S. Olson, S. W. Bidwell, W. C. Boncyk, and S. Ameen, 1996: Structure of Florida thunderstorms using high-altitude aircraft radiometer and radar observations. *J. Appl. Meteor.*, **35,** 1736–1762.

Hitschfeld, W., and J. Bordan, 1954: Errors inherent in the radar measurement of rainfall at attenuating wavelengths. *J. Meteor.,* **11,** 58–67.

Jones, J. A., R. Meneghini, T. Iguchi, and W.-K. Tao, 1997: Synthetic data for testing TRMM radar algorithms. Preprints, *28th Conf. on Radar Meteorology,* Austin, TX, Amer. Meteor. Soc., 196–197.

Kummerow, C., and Coauthors, 2000: The status of the Tropical Rainfall Measuring Mission (TRMM) after two years in orbit. *J. Appl. Meteor.,* **39,** 1965–1982.

Lenoble, J., Ed.,1985: *Radiative Transfer in Scattering and Absorbing Atmospheres: Standard Computational Procedures.* A. Deepak, 300 pp.

Marshall, J. S., and W. M. Palmer, 1948: The distribution of raindrops with size. *J. Meteor.,* **5,** 165–166.

Marzano, F. S., A. Mugnai, G. Panegrossi, N. Pierdicca, E. A. Smith, and J. Turk, 1999: Bayesian estimation of precipitating cloud parameters from combined measurements of spaceborne microwave radiometer and radar. *IEEE Trans. Geosci. Remote Sens.*, **37,** 596–613.

McFarquhar, G. M., and A. J. Heymsfield, 1997: Parameterization of tropical cirrus ice crystal size distributions and implications for radiative transfer: Results from CEPEX. *J. Atmos. Sci.,* **54,** 2187–2200.

Meneghini, R., H. Kumagai, J. R. Wang, T. Iguchi, and T. Kozu, 1997: Microphysical retrievals over stratiform rain using measurements from an airborne dual-wavelength radar–radiometer. *IEEE Trans. Geosci. Remote Sens.,* **35,** 487–506.

Nelder, J. A., and R. Mead, 1965: A simplex-method for function minimization. *Comput. J.,* **7,** 308–313.

Olson, W. S., C. D. Kummerow, G. M. Heymsfield, and L. Giglio, 1996: A method for combined passive–active microwave retrievals of cloud and precipitation profiles. *J. Appl. Meteor.,* **35,** 1763–1789.

Racette, P., R. F. Adler, J. R. Wang, A. J. Gasiewski, D. M. Jackson, and D. S. Zacharias, 1996: An airborne Millimeter-Wave Imaging Radiometer for cloud, precipitation, and atmospheric water vapor studies. *J. Atmos. Oceanic Technol.,* **13,** 610–619.

Sauvageot, H., 1996: Retrieval of vertical profiles of liquid water and ice content in mixed clouds from Doppler radar and radiometer measurements. *J. Appl. Meteor.,* **35,** 14–23.

Savov, P. B., T. S. Skakalova, I. N. Kolev, and F. L. Ludwig, 2002: Lidar investigation of the temporal and spatial distribution of atmospheric aerosols in mountain valleys. *J. Appl. Meteor.,* **41,** 528–541.

Sekhon, R. S., and R. Srivastava, 1970: Snow size spectra and radar reflectivity. *J. Atmos. Sci.,* **27,** 299–307.

Sihvola, A. H., 1989: Self-consistency aspects of dielectric mixing theories. *IEEE Trans. Geosci. Remote Sens.,* **27,** 403–415.

Simpson, J., C. Kummerow, W.-K. Tao, and R. F. Adler, 1996: On the Tropical Rainfall Measuring Mission (TRMM). *Meteor. Atmos. Phys.,* **60,** 19–36.

Skofronick-Jackson, G. M., and A. J. Gasiewski, 1995: Nonlinear statistical retrievals of ice content and rain rate from passive microwave observations of a simulated convective storm. *IEEE Trans. Geosci. Remote Sens.,* **33,** 957–970.

——, ——, and J. R. Wang, 2002: Influence of microphysical cloud parameterizations on microwave brightness temperatures. *IEEE Trans. Geosci. Remote Sens.,* **40,** 187–196.

Spencer, R. W., R. E. Hood, F. J. LaFontaine, E. A. Smith, R. Platt, J. Galliano, V. L. Griffin, and E. Lobl, 1994: High-resolution imaging of rain systems with the advanced microwave precipitation radiometer. *J. Atmos. Oceanic Technol.,* **11,** 849–857.

Tao, W.-K., and J. Simpson, 1993: Goddard cumulus ensemble model. Part I: Model description. *Terr. Atmos. Oceanic Sci.,* **4,** 35–72.

van de Hulst, H. C., 1980: *Multiple Light Scattering: Tables, Formulas, and Applications.* Vol. 2. Academic Press, 436 pp.

Viltard, N., C. Kummerow, W. S. Olson, and Y. Hong, 2000: Combined use of the radar and radiometer of TRMM to estimate the influence of drop size distribution on rain retrievals. *J. Appl. Meteor.,* **39,** 2103–2114.

Wang, Z., and K. Sassen, 2002: Cirrus cloud microphysical property retrieval using lidar and radar measurements. Part I: Algorithm description and comparison with in situ data. *J. Appl. Meteor.,* **41,** 218–229.